AI-Enabled Materials Design of Non-Periodic 3D Architectures With Predictable Direction-Dependent Elastic Properties

Deng, Wen Jing; Kumar, Siddhant; Vallone, Alberto; Kochmann, Dennis M.; Greer, Julia R.

DOI
10.1002/adma.202308149

Publication date
2024

Document Version
Final published version

Published in
Advanced Materials

ADVANCED MATERIALS
www.advmat.de

AI-Enabled Materials Design of Non-Periodic 3D Architectures With Predictable Direction-Dependent Elastic Properties

*Weiting Deng, Siddhant Kumar, Alberto Vallone, Dennis M. Kochmann, and Julia R. Greer**

Natural porous materials have exceptional properties—for example, light weight, mechanical resilience, and multi-functionality. Efforts to imitate their properties in engineered structures have limited success. This, in part, is caused by the complexity of multi-phase materials composites and by the lack of quantified understanding of each component's role in overall hierarchy. This challenge is twofold: 1) computational. because non-periodicity and defects render constructing design guidelines between geometries and mechanical properties complex and expensive and 2) experimental. because the fabrication and characterization of complex, often hierarchical and non-periodic 3D architectures is non-trivial.

1. Introduction

Porous materials are omnipresent in natural and artificial objects. Natural porous media exhibit a broad range of length scales and geometries, from nano- to micro- to macro-scale. For example, **Figure 1** shows the images (top row) and corresponding microstructures (bottom row) of a diatom, a peacock feather, a trabecular bone, and a sea sponge, which have columnar, lamellar, cubic, and isotropic topologies, respectively (insets, Figure 1, bottom row). Porous materials are critical to multiple engineering fields, such as conversion and storage of energy,[1–3] biomedical pursuits (scaffolds for tissue formation and organoids,[4] drug delivery carriers,[1] etc.), materials engineering,[5] environmental engineering (water purification,[6] gas sensing,[7] etc.), chemical engineering[2] (catalysis and photocatalysis, etc.), civil engineering[8] (concrete, metal foam, etc.), and optical applications (porous silicon[9]).

Multiple attempts to develop strategies for mimicking natural porous geometries have been made to engineer materials with superior properties and performance. Emulating the constructs of natural materials is not trivial, especially for the non-periodic and disordered topologies, which typically support a combination of mechanical, chemical, and biological functions. Some reported strategies to generate stochastic aperiodic porous structures include random tessellation techniques such as the Voronoi tessellation model,[10] which generates structures through frames that are defined by random discrete points in 3D space; Laguerre tessellations,[11] which define the skeleton of open-cell foams via random sphere packing;[12] and other non-periodic designs such as the hexahedral mesh refinement approach[13] and the adaptive rhombic grid method[14] that can control pore size distribution and comply with manufacturing requirement. A particular 3D pattern, called spinodal decomposition (**Figure 2**), has attracted attention in the architectural design field due to its tunability[15,16] and exceptional mechanical properties.[17,18] The early kinetic evolution of spinodal decomposition is described by the Cahn–Hilliard-type phase field equations,[19–21] which are computationally expensive to solve. To add tunability to mechanical anisotropy, Vidyasagar et al. first employed anisotropic surface energies to adjust the anisotropic elastic moduli of resulting microstructures.[15] Soyarslan et al. applied a Gaussian random field as a close approximation to achieve a stochastically porous microstructure with tunability in anisotropy and porosity.[22] The existing porous structural models were, however, incapable of predicting optimal microstructural architectures of self-connected porous geometries with controlled and valid anisotropy, pore shape, and porosity.

Fabricating biomimetic materials has always been challenging due to their intricate 3D structural architectures, which far exceed the capabilities of conventional fabrication techniques. Additive manufacturing (AM) has opened up new possibilities for manipulating and imitating the naturally multiscale and

W. Deng, J. R. Greer
Division of Engineering and Applied Sciences
California Institute of Technology
Pasadena, CA 91125, USA
E-mail: jrgreer@caltech.edu

S. Kumar
Department of Materials Science and Engineering
Delft University of Technology
Delft 2628 CD, The Netherlands

A. Vallone, D. M. Kochmann
Department of Mechanical and Process Engineering
ETH Zurich
Zurich 8092, Switzerland

J. R. Greer
Kavli Nanoscience Institute at Caltech
Pasadena, CA 91125, USA

The ORCID identification number(s) for the author(s) of this article can be found under https://doi.org/10.1002/adma.202308149

DOI: 10.1002/adma.202308149

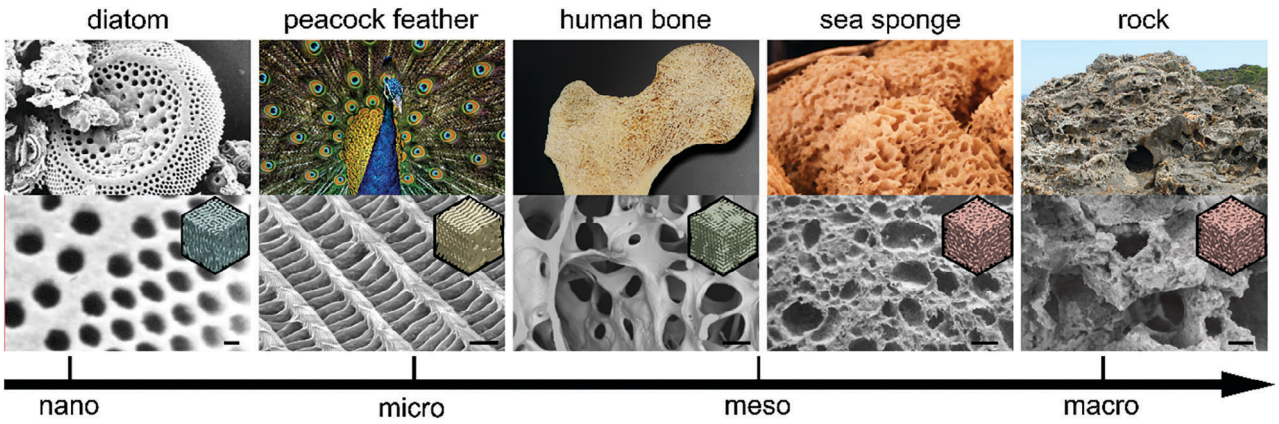

Figure 1. Overview of natural porous materials, placed alongside the length scale from nano- to macro-scale according to their critical dimensions. The SEM or OM images of the original porous structures are shown from left to right: diatom, peacock feather, human bone, sea sponge, and rock. Insets in the microstructure images are spinodoids with similar topology: columnar, lamellar, cubic, and isotropic spinodoids. Images reproduced with permission: diatom image[36] is licensed under CC BY 3.0; peacock feather images[37,38] are licensed under CC BY-SA 4.0 and CC BY-SA 3.0; human bone[39] copyright 2003 John Wiley & Sons; sea sponge[40] is licensed under CC BY-SA 3.0; all other images are original or free licensed; scale bar: 500 nm, 1 µm, 500 um, 1.5 mm, and 3 cm.

multifunctional structures.[23] For example, S. Frolich et al. utilized a vat polymerization 3D printer to investigate a brick-and-mortar-like architecture design inspired by mollusk nacre;[24] M. Wehner et al. fabricated an octopus-inspired autonomous robot using an embedded 3D printing technique[25] and Senhora, et al manufactured some complex spinodal systems.[26] Despite the rapid development of this field, the absence of nondestructive testing methods for printing flaws and structural integrity,[27] which have a substantial impact on the mechanical properties of porous metamaterials, continues to be a great obstacle.

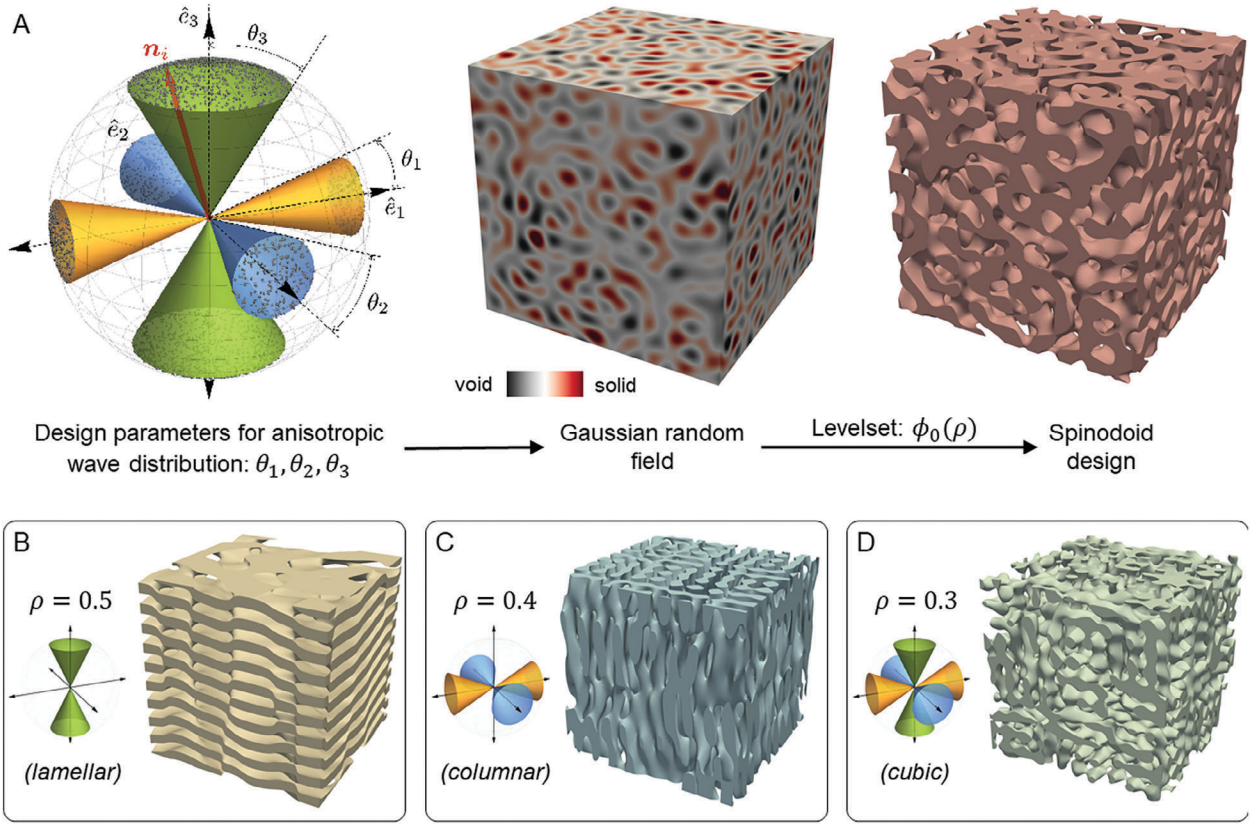

Figure 2. Demonstration of spinodoid structures. A) Illustration of anisotropic spinodoid generation process. B–D) Representative spinodoids with lamellar, columnar, and cubic topologies.

Manufacturing imperfections further complicate the procedure of obtaining architectures with requisite anisotropy.

In this work, we leverage the combination of machine learning algorithms and two-photon lithography additive manufacturing to design and fabricate 3D spinodoids with structural similarity and mechanical analogy to trabecular bone, which is challenging to imitate due to its structural complexity and mechanical anisotropy. We first apply a Gaussian random field model[22] to construct a spinodoid topology, similar to spinodal decomposition, and then apply a forward machine learning algorithm to predict the stiffness tensor, whose accuracy is verified by nanomechanical experiments. We then employ an inverse neural network algorithm to produce spinodoid structures with targeted anisotropic elastic moduli. These 3D scaffolds with spinodoid architectures of micro-level dimensions ($70 \times 70 \times 70\ \mu m^3$) were fabricated by a two-photon lithography technique out of an IP-Dip photoresist. Our experiments reveal that the morphologies of the two-photon lithography-fabricated scaffolds closely matched that of trabecular bone which was used as a query for the inverse model. The stiffnesses anisotropy of the 3D structures closely matched the predictions of the machine learning framework based on the artificial neural networks. This work demonstrates the capability and efficiency of utilizing AI models to generate complex, non-periodic 3D shapes that also have the AI-predicted desired mechanical property landscape, in additive manufacturing of advanced hierarchical materials, that is, ones whose fundamental building blocks are on the order of microstructurally relevant length scales, nanometers, and microns.

2. Computational Design Via Deep Learning

2.1. Spinodoid Design Space

Spinodoid[22,27] metamaterials are based on a close approximation of the phase-field observed in the early stage of spinodal decomposition, commonly described by the Cahn–Hilliard model.[19–21] They consist of smooth, non-intersecting, and bicontinuous surfaces that minimize stress concentrations and exhibit mechanical resilience superior to truss- and plate-based metamaterials.[17,28] These surfaces are also doubly-curved, which serves to preferentially stretch the material instead of bending it, rendering the scaling of stiffness and strength with respect to density linearly[17,28] and better fatigue resistance.[29] We define the spinodoid topology using a mathematical function shown in Equation (1) in $\boldsymbol{x} \in \Omega$ domain via an anisotropic Gaussian random field $\phi : \Omega \rightarrow \mathbb{R}$. The Gaussian random field is described by a summation of $N \gg 1$ random standing waves with a fixed wavenumber, $\beta > 0$ as:

$$\phi\ (x) = \sqrt{\frac{2}{N}}\ \sum_{i=1}^{N} \cos\left(\beta \boldsymbol{n}_i\ \cdot \boldsymbol{x} + \gamma_i\right) \tag{1}$$

where $\boldsymbol{n}_i \in S(2)$ represents the random wave-vector directions sampled from the unit sphere $S(2)$ and $\gamma_i \approx \mathcal{U}(0, 2\pi)$ describes uniformly sampled phase angles. The microstructural length scale is given by the wavelength $2\pi/\beta$ and can be chosen to be arbitrarily small (practically, the smallest number is limited by the machine accuracy of computers). The probability distribution of the wave directions $\boldsymbol{n}_i$ in $S(2)$ determines the anisotropy of the Gaussian random field. Vidyasagar et al.[15] and Kumar et al.[27] showed that anisotropy in this distribution can be a product of the anisotropy in the surface energy or mobility, respectively, of the underlying spinodal decomposition process. The latter showed that such distribution can be obtained using only three parameters: $\{\theta_1, \theta_2, \theta_3\} \in [0, \pi/2]^3$, which approximates the probability distribution of the standing wave-vectors as three mutually orthogonal pairs of cones diverging from the origin (Figure 2A). The wave-vectors are uniformly and randomly sampled from within these cones in $S(2)$. Applying a level set given by $\phi_0 = \sqrt{2}\ \mathrm{erf}^{-1}(2\rho - 1)$, where $\phi \leq \phi_0$ corresponds to smooth solid regions and to voids otherwise, offers a straightforward control of the relative density, $\rho \in [0, 1]$ within the sample, independent of its inherent anisotropy. This combination of four design parameters, $\{\rho,\ \theta_1, \theta_2, \theta_3\}$, covers a large and diverse property space, including a wide range of anisotropic stiffness responses (Figure 2B–D). The absence of long- and short-range order in spinodoids offers seamless function grading and avoids symmetry-breaking defects, both of which are active challenges in lattices and other periodic truss- or plate-based structure designs.

2.2. Inverse Design Via Deep Learning for Tailored Anisotropy

Most state-of-the-art biomimetic metamaterials with special properties are currently designed using an interactive trial-and-error-based exploration of the structure–property maps.[30] We leverage a machine-learning framework (details in Section S1, Supporting Information) to invert the structure–property relations of spinodoid metamaterials and design scaffolds with tailored anisotropic stiffness using minimal computational resources.[31] **Figure 3** depicts the algorithm of this process in the context of inverse-designed bone scaffolds that locally match the anisotropic stiffness of a trabecular bone. This can eventually help develop better bone scaffolds, which for example, can suppress stress shielding in future orthopedic implants.

The deep learning framework is based on a combination of two neural networks (NN) – a forward model that maps spinodoid design, described by $\{\rho,\ \theta_1, \theta_2, \theta_3\}$, onto the respective anisotropic stiffness, described by a fourth-order tensor, and an inverse model that takes the target anisotropic stiffness as input and efficiently predicts a possible spinodoid design with the target stiffness (see Section S1, Supporting Information for details). The inverse model operates on the entire 3D anisotropic stiffness tensor, not just on the three principal Young's moduli. In contrast to optimization-based design strategies (e.g., using Bayesian optimization), which are sensitive to the choice of initial guess and need to be re-run for every design task, the inverse model (only after it has been trained) may be perceived as a zero-shot and instant optimizer for all possible design tasks by virtue of analyzing the entire property space through a dataset. The machine learning model is trained purely on the data pertaining to spinodoid metamaterials and is able to accurately extrapolate it to bone data and, in principle, to any shape with arbitrary orthotropic stiffness. This is important because training data is scarcely available for biological structures such as bone.[30] We demonstrate the efficacy of this machine learning framework to design spinodoid-based synthetic bone by obtaining precise matching of predicted

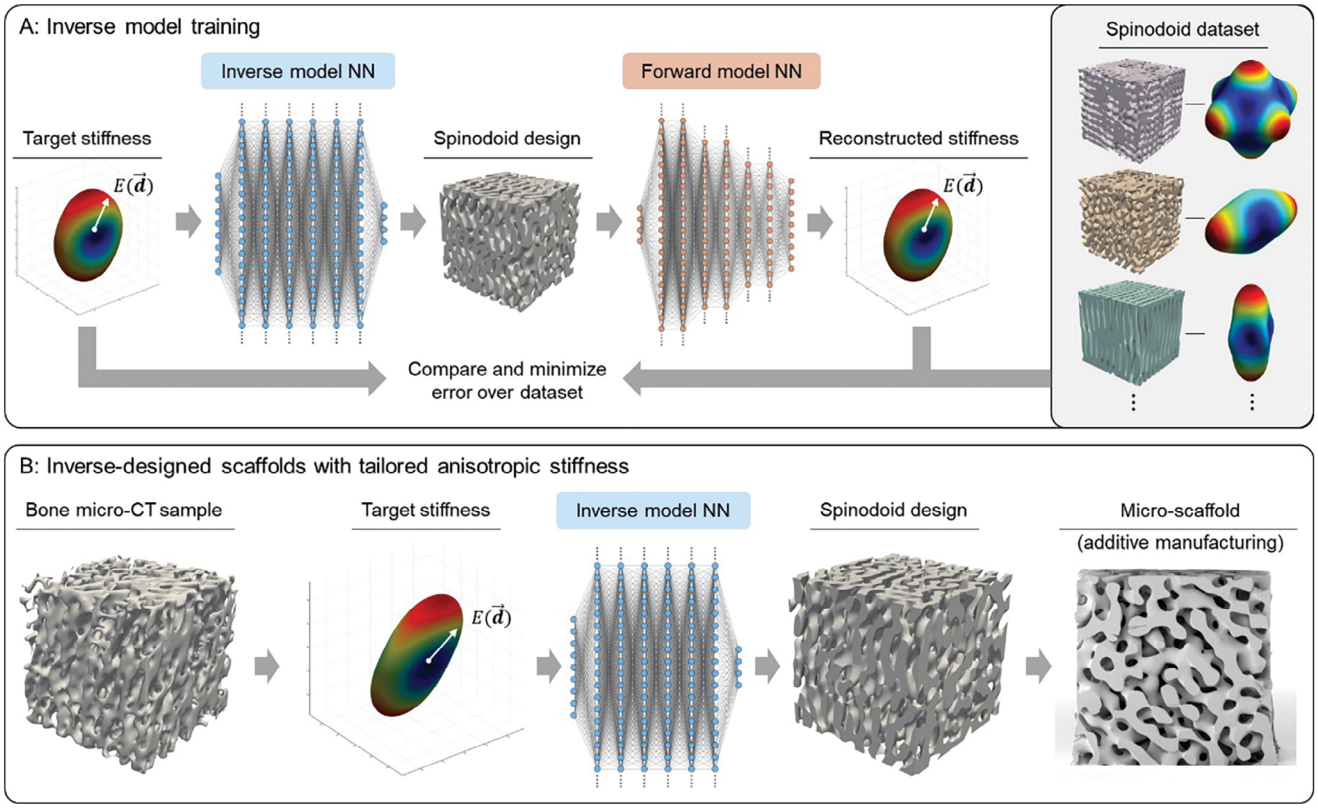

Figure 3. Schematics of the inverse design of spinodoid structure via deep learning. A) The inverse model NN takes a target 3D anisotropic stiffness as input and predicts a spinodoid design. The output is a reconstructed spinodoid stiffness generated by the forward model NN. Both NNs are trained on a representative dataset consisting of spinodoid design parameters and corresponding anisotropic stiffness computed via the finite element method. B) Schematic of designing a spinodoid scaffold with stiffness matching with a trabecular bone. A 3D micro-CT image of a trabecular bone sample is converted into a finite element model to compute a target 3D anisotropic stiffness. The inverse model NN then predicts a spinodoid design that matches the target stiffness, which is then additively manufactured.

anisotropy with the analyzed results for 127 trabecular bone samples extracted from the femoral head of 32 human patients,[32] of which a representative example is shown in Figure 3 (see Section S2, Supporting Information for details and quantitative analysis). We highlight that this framework can predict functionally graded spinodoid metamaterials that locally match those of non-periodic heterogeneous structures, for example, heterogeneous trabecular bone (see Figure S7, Supporting Information). While the presented frameworks use deterministic neural networks that only predict one design for a target property, future extension to generative and stochastic machine learning models (albeit at the expense of complexity) opens the possibility to obtain multiple designs for the same target property and enable secondary design considerations such as ease of manufacturing and cost.

3. Additive Manufacturing and Nanomechanical Experiments

3.1. Forward Model Prediction Accuracy

To experimentally explore the prediction accuracy of the forward model, we fabricated several representative computed architectures using two-photon lithography direct laser writing out of IP-Dip photoresist (Nanoscribe GmbH). Details of this fabrication process are provided in the Experimental Section. The samples had the design parameter set as {0.4°, 15°, 45°, and 30°}, which produced topologies with cubic form factors, the overall dimensions of 70 × 70 × 70 μm^3, the wavenumber $\beta = \frac{30\pi}{70}$ μm^{-1}, and pore size of ~2 um defined by wavenumber. **Figure** 4A contains a SEM image of a representative fabricated anisotropic spinodoid sample. The mechanical anisotropy of this structure is highlighted by the computed elastic surface, shown in Figure 4B, which conveys the orientation-dependent sample stiffness. We obtained the full elastic tensor $\mathbb{C}$ of the geometry via the forward model, and then, extracted the compliance tensor $\mathbb{C}^{-1}$, which provided Young's modulus $E(\boldsymbol{d})$ along each direction given by unit vector $\boldsymbol{d} \in S(2)$ as $E^{-1}(\boldsymbol{d}) = \sum_{i=1}^{3}\sum_{j=1}^{3}\sum_{k=1}^{3}\sum_{l=1}^{3}\mathbb{C}^{-1}_{ijkl}d_i d_j d_k d_l$. We then normalized the obtained moduli by the maximum directional Young's modulus ($\frac{E(\boldsymbol{d})}{E_{\max}}$). We found that for this architecture, the largest orientation stiffness occurred along the $\hat{\boldsymbol{e}}_1$ direction, with the color-intensity contour plot shown in Figure 4B. This plot reveals a high anisotropy range of 0.36 to 1.00, with the predicted normalized Young's moduli of 0.360 in $\hat{\boldsymbol{e}}_2$ and of 0.621 in $\hat{\boldsymbol{e}}_3$ directions.[33]

We conducted in situ nanomechanical experiments on the fabricated samples in a custom nanomechanical instrument, SEMentor[34] (Quanta 200 FEG, Thermo Fisher), with a

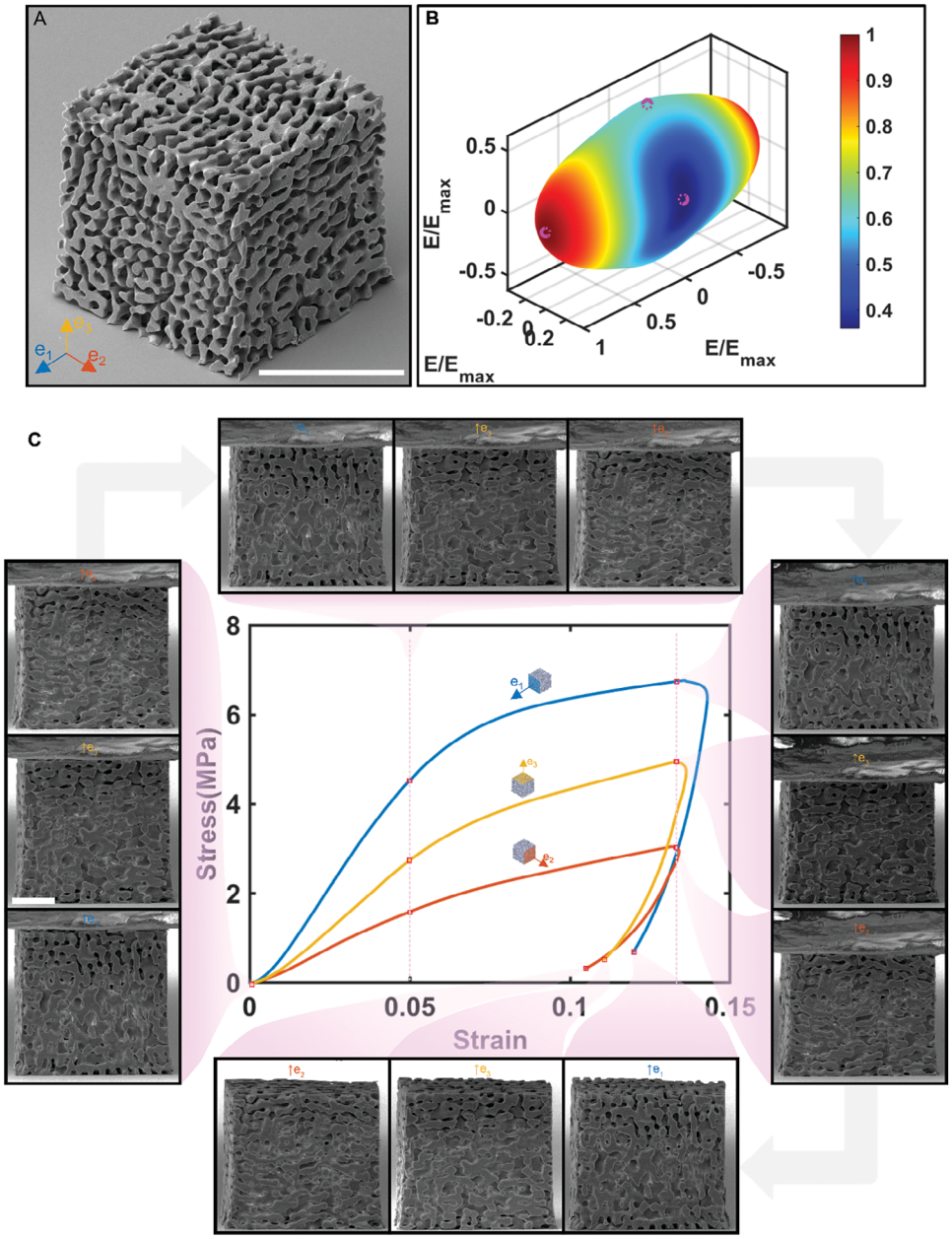

Figure 4. Experimental verification of the forward model accuracy. A) SEM image of a representative spinodoid sample. Scale bar: 40 μm. B) Surface plot of normalized effective elastic modulus of the sample; magenta circles represent experimental results collected via ex situ quasi-static compression tests. C) In situ quasi-static compressive stress versus strain data on one representative configuration in three orthogonal orientations. The data set of each color corresponds to the compression orientation. Scale bar: 20 μm.

170 μm-diameter flat diamond tip at a strain rate of 10^{-3} s^{-1} along the three mutually orthogonal $\hat{e}_1$, $\hat{e}_2$, and $\hat{e}_3$ directions. To account for the stochastic design of spinodoids, we computationally generated three or more configurations with the same design parameters but different random seeds. In addition to the in situ experiments, we also compressed a minimum of five identical samples in each direction in a nanoindenter (G200 XP; KLA) with a 120 μm-diameter flat punch, resulting in at least fifteen samples being tested for each configuration (details of ex situ uniaxial compression experiments are provided in the Experimental Section). Figure 4C contains a representative experimental stress–strain response computed by normalizing the load versus displacement measurements by the initial sample geometry. It demonstrates that the spinodoid samples compressed along the $\hat{e}_2$ and $\hat{e}_3$ orientations exhibited linear loading up to a strain of ≈5%; the sample in $\hat{e}_1$ direction deformed linearly prior to ≈4% strain. The effective elastic moduli were computed from the stress–strain slopes of the linear loading regime and normalized by the measured stiffness in the $\hat{e}_1$ direction of the corresponding sample. For the representative example in Figure 4, the effective

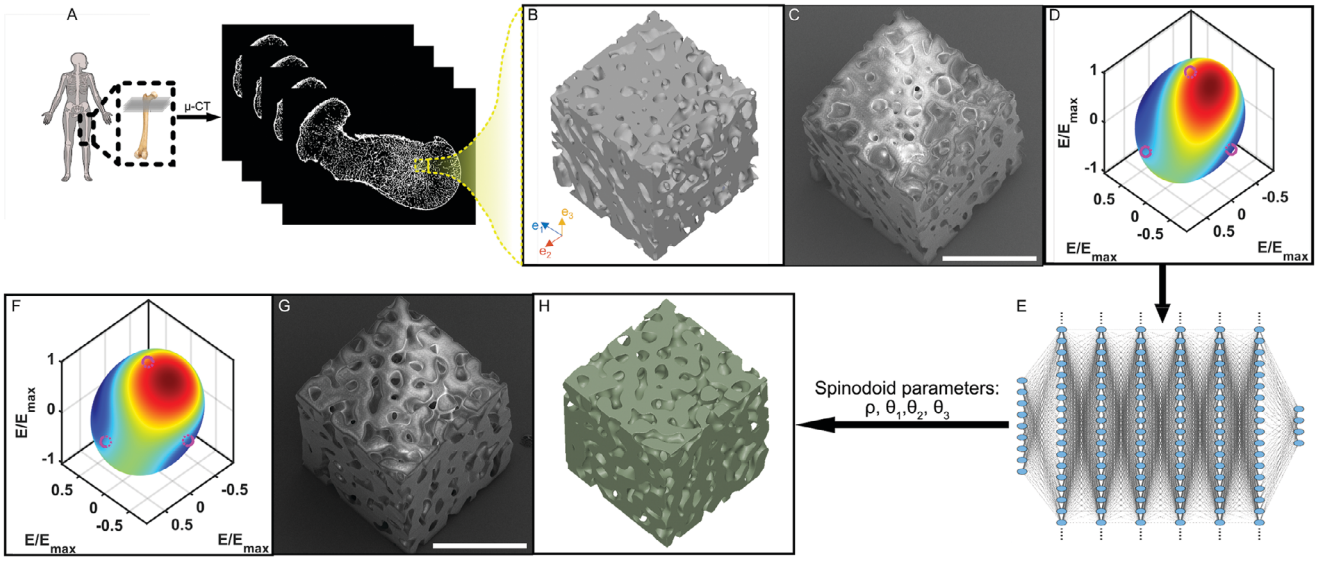

Figure 5. Application of the inverse model to resemble a human femur bone. A) Extracting 3D trabecular bone structure from μ-CT data. B) 3D structure of an extracted bone sample. C) SEM image of additively manufactured bone sample. D) Surface plot of the effective elastic modulus of the bone sample. E) The inverse model NN: using the stiffness of the bone sample as input. F) Surface plot of the effective elastic modulus of the spinodoid sample, and the magenta circles present the experimental results. G) SEM image of the additively manufactured spinodoid. H) 3D structure of the corresponding spinodoid generated by the inverse model. Scale bar: 40 μm.

normalized elastic moduli in $\hat{e}_1$, $\hat{e}_2$, and $\hat{e}_3$ directions were measured to be 1.00 ± 0.10, 0.35 ± 0.04, and 0.6 ± 0.10. The plot in Figure 4B also contains the experimental results overlaid onto the computed 3D contours, plotted as magenta circles, and indicate reasonable agreement with deep learning-based prediction of 1.00, 0.36, and 0.62. The SEM images of Figure 4C contain detailed deformation characteristics of this representative sample during quasi-static compressions. We chose to image the sample at four distinct strains: 0%, which marks the intact sample; 5%, which represents a transition from linear regime to non-linearity; 13%, which marks the end of the loading; and ≈10–12%, which is the final post-compression strain. These images convey that the samples maintained structural integrity throughout the deformation, including the linear-to-non-linear transition point, and contained local fractures at the end point of the loading. An additional set of experimental results is presented in Section S3.1, Supporting Information.

3.2. Inverse Design for Anisotropy Matching With Femoral Bone

To demonstrate the accuracy and efficiency of the inverse design framework, we applied this model to generate a spinodoid geometry that is similar to trabecular bone, whose stiffness tensor matches that of a cubic trabecular bone sample extracted from a human proximal femur (these geometries were obtained from micro-computed tomography [micro-CT] data using an open-source software 3D Slicer (**Figure** 5A)). The stiffnesses of the bone samples was computed using ABAQUS simulations (see Section S2, Supporting Information for more details). The computed stiffness tensor was used as a query for the inverse-design neural network to predict the spinodoid design parameters with the targeted anisotropic stiffness. Figure 5B shows the reconstructed bone geometry, and Figure 5H contains the model-predicted spinodoid shape, with a wavenumber $\beta = \frac{15\pi}{70}$ μm^{-1} (chosen to mimic the pore size of trabecular bone), that was used to print the IP-Dip samples. Figure 5C,G contains SEM images of these two types of samples, and Figure 5D contains the computed elastic surface of the bone architecture, calculated as $E^{-1}(\boldsymbol{d}) = \sum_{i=1}^{3}\sum_{j=1}^{3}\sum_{k=1}^{3}\sum_{l=1}^{3}\mathbb{C}^{-1}_{ijkl}d_i d_j d_k d_l$. The compliance tensor $\mathbb{C}^{-1}_{\text{bone}}$ was computed from the numerically calculated stiffness tensor $\mathbb{C}_{\text{bone}}$. The bone samples may not necessarily align with the coordinate system. For the representative bone sample in Figure 5, we found the direction of the maximum modulus ($E_{\max}$) to be $\boldsymbol{d} = [-0.384,\ 0,\ 0.923]^T$. For consistency, we normalized the moduli of the bone sample by the modulus in $\hat{e}_3$ direction, the largest among the three orthogonal orientations as numerically calculated by ABAQUS, which yielded the moduli ratio of $E_{\text{bone},\hat{e}_1} : E_{\text{bone},\,e_2} : E_{\text{bone},e_3} = 0.82 : 0.85 : 1.00$. Quasi-static compression experiments revealed the elastic moduli in $\hat{e}_1$, and $\hat{e}_2$ directions, normalized by that in $\hat{e}_3$, to be 0.84 ± 0.02 and 0.91 ± 0.02, shown as circle data markers in Figure 5D. The solid and the dashed outlines of the magenta circles in the figure indicate the intersection of data with the computed elastic surface and the accuracy of the stiffness tensor prior to its application to the inverse-design model. The stiffness tensor $\mathbb{C}_{\text{bone}}$ was used as a query for the inverse-design neural network, which predicted the spinodoid design with the targeted anisotropic stiffness $\mathbb{C}_{\text{spin}}$. More details on the analysis and prediction method can be found in Section S2.1, Supporting Information. Figure 5F contains the directional stiffness of the generated spinodoid sample normalized by its maximum value ($\frac{E(\boldsymbol{d})}{E_{\max}}$), at $\boldsymbol{d} = [-0.417,\ 0.015,\ 0.908]^T$. The inverse model (via the forward model) predicted the axial moduli normalized by $E_{\text{spin},\hat{e}_3}$ along $\hat{e}_1$, $\hat{e}_2$, and $\hat{e}_3$, respectively, to be 0.82, 0.85, and 1.0, virtually equivalent to the experimental

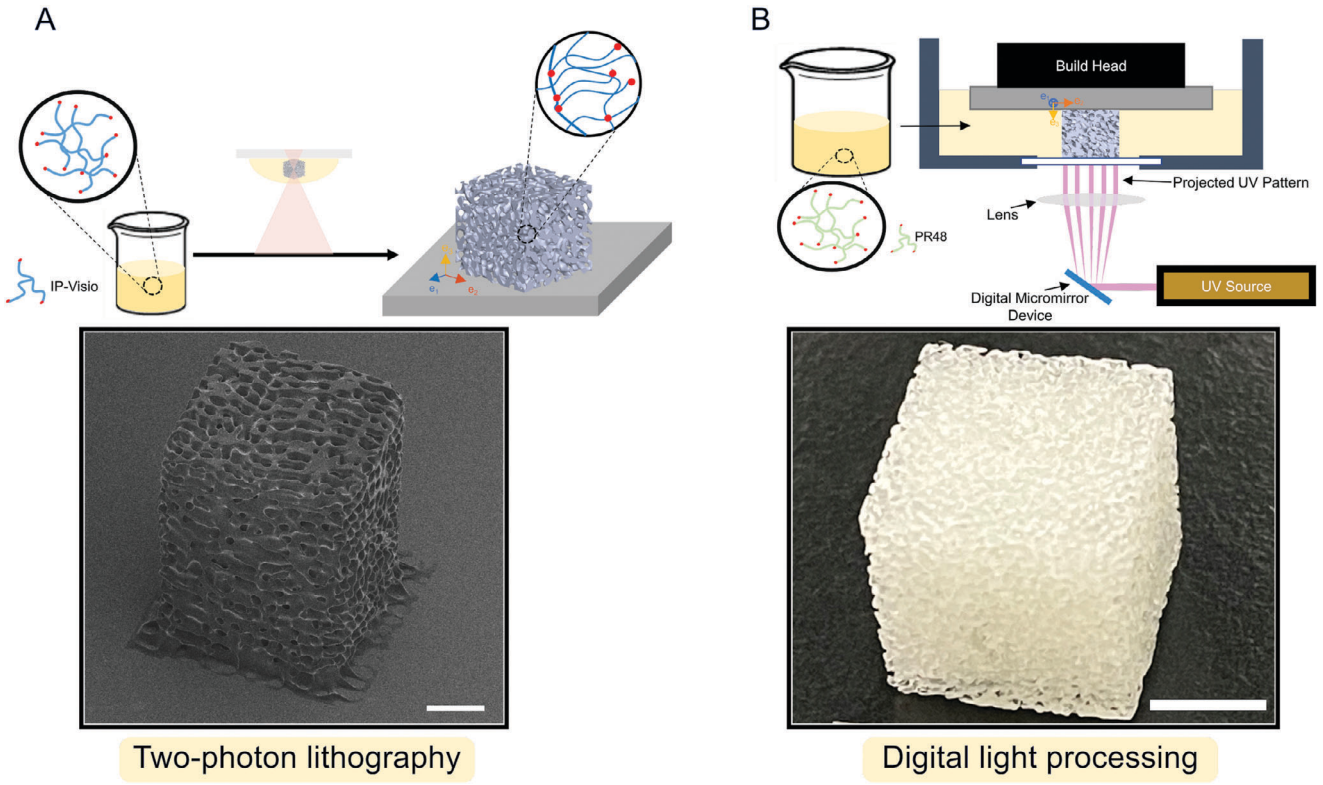

Figure 6. Demonstration of spinodoid printability using different 3D-patterning techniques. A) Schematic of the two-photon lithography (TPL) process and a SEM image of a representative spinodoid sample printed with IP-Visio resist. Scale bar: 100 µm. B) Schematic of digital light printing (DLP) process and an optical image of the spinodoid sample printed with PR48 resist. Scale bar: 5 mm.

results: 0.81 ± 0.14, 0, 84 ± 0.15, and 1.00 ± 0.16. The resemblance between the elastic surface plots of the bone and the spinodoid samples demonstrates that the inverse neural network model was capable of predicting a particular structure with requisite anisotropic stiffness features and that these architectures could be additively manufactured.

3.3. Generality and Customizability

We demonstrate the applicability of this framework to a broad range of additive manufacturing techniques, length scales, and materials by fabricating samples with architectures generated by models at the nano-, micro-, and macro-scale. We used two-photon lithography with a biocompatible non-cytotoxic photoresist, IP-Visio, to manufacture samples with an overall dimension of 300 µm × 300 µm × 300 µm and critical features of 20 µm, shown in **Figure 6**A. The sample maintained structural integrity through the fabrication process, with a marginal volumetric shrinkage during the drying step (see Experimental Section). We chose this sample size to be on the order of some living cells, for example, fibroblasts and osteoblasts, to highlight the potential application of this AI-informed AM in cell-related research, that is, 3D cell niches.[35] We also used a digital light processing 3D printer (Autodesk Ember) to fabricate cm-scale samples out of a standard commercial resin, PR48, as shown in Figure 6B.

4. Discussion and Outlook

We present a framework for designing and fabricating complex, non-periodic porous structures with precise controllability and large tunability of direction-specific effective elastic moduli, porosity, and architecture. The structure design is a close approximation of the spinodal decomposition process, defined by Equation (1), and we coin it as spinodoid topology. As a proof of concept, samples in this work are topologically and mechanically comparable to the porous geometry of cancellous bones, whose stiffness tensor is fully quantified.

We utilize an AI-based forward model to predict the directional-dependent stiffness of a designed spinodoid sample, which is validated by uniaxial compression experiments of samples with identical design parameters fabricated using the two-photon lithography. This accuracy is reached by using the wavenumber $\beta = \frac{30\pi}{70}$ µm^{-1}, a factor of 1.5 greater than the training data used in the machine learning training process. This implies that the neural network method developed in this work can enable the precise mimicry of complex 3D architectures with built-in anisotropy. A more detailed discussion on the effects of wavenumber and relative density on the prediction accuracy of the deep learning-based forward model is provided in Section S3.2, Supporting Information.

The similarity between the inverse model predicted spinodoid structure and the bone architecture reconstructed from tomography slices (Figure 5) indicates three key outcomes. First, the deep

learning framework is capable of successfully designing a spinodoid whose non-periodic, complex topology resembles the target trabecular network and orientation. Second, the anisotropic stiffness of the computed spinodoid matches that of the bone, with the expected minor differences that arise from the non-zero normal-shear coupling in the bone sample,[27] discretization errors in surfaces extraction from micro-CT data of the bone samples, and inevitable imperfections introduced during the additive manufacturing process. Third, the inverse model achieves topological and mechanical analogy with the bone sample built on a fully bone-agnostic data set in the training step, which signifies that the presented machine learning-enabled prediction framework can predict a wide range of porous architectures with targeted elastic properties in all directions. This methodology is applicable to spatially-graded designs with locally matching anisotropic stiffness, as shown in Figure S6, Supporting Information. Beyond stiffness, our experiments on spinodoids illustrate that the mechanical anisotropy spans to the post-elastic regime; more detailed descriptions and discussion are shown in Section S3.3, Supporting Information.

The choice of the model sample design and the fabrication framework in this work are inspired by the complexities and challenges of the natural aperiodic porous topologies. These designing framework and additive manufacturing methods are not limited to a single architecture, that is, a bone scaffold, and can be easily adapted to a variety of applications, such as biomedicine engineering,[1] environmental engineering,[7] and energy engineering.[2,3] The broad versatility of multi-scale, hierarchical architectures that can be predicted by the presented AI-based model and fabricated using a 3D printing setup, with feature resolution from nano- to micro- and macro-level scale, provides a pathway to produce samples with stochastic porous morphologies that can be fully quantified and topologically designed to resemble their natural counterpart. It broadens and populates the new design space of meta-materials, with more controllability in predictable anisotropy, which is conventionally complicated.

5. Experimental Section

Microscale Sample Fabrication: The computed geometries were fabricated at the microscale using a two-photon lithography process in a commercially available system (Photonic Professional GT, Nanoscribe GmbH) using a Zeiss Plan Apochromat 63X/1.4 Oil DIC objective. Rastering of the laser was obtained by a set of galvo-mirrors and piezoelectric actuators. The writing parameters were a slicing distance of 0.2 µm and a hatching distance of 0.2 µm. Laser power was 15 mW and scan speed was 10 mm s^{-1} on an IP-Dip photoresist. The structures were written on a cleaned silicon chip substrate via two-photo lithography of size 70 µm × 70 µm × 70 µm. To guarantee thorough development, the printed samples were developed in PGMEA (propylene glycol methyl ether acetate, Sigma–Aldrich) for more than 12 h and rinsed with ultra-purified isopropyl alcohol (Sigma–Aldrich). To prevent excessive warping during the developing process, the samples were dried using a critical point drying process in an Autosamdri-931 system (Tousimis) using ultra-purified isopropyl alcohol.

Scanning Electron Microscope (SEM) Imaging and In Situ Nanomechanical Experiments: The fabricated samples were compressed using a 170-µm diamond flat punch tip affixed to a nanoindenter (InSEM II from Nanomechanics Inc.) installed in an SEM chamber (FEI Quanta 200F) that allowed for in situ imaging of the sample during the compression test. Samples were imaged in SEM at 2 kV to mitigate polymer surface charging phenomena. The compressions were done at room temperature at a pressure of ≈10^{-5} mbar at a global strain rate of $\dot{\varepsilon} = 10^{-3}$ s^{-1}, controlled by a feedback algorithm for these fabricated samples.

Ex Situ Quasi-Static Compression: Ex Situ nanoindentation experiments were carried out for additional data collection. Nanomechanical experiments were performed on the spinodoid architectures to determine their effective stiffness along the $\hat{e}_1$, $\hat{e}_2$, and $\hat{e}_3$ directions. Ex situ uniaxial compression experiments were performed on a minimum of five samples per direction and three configurations of the same generation parameter set $\Theta = \{\rho, \theta_1, \theta_2, \theta_3\}$ using a G200 XP Nanoindenter (KLA). The samples were compressed to strains of $\dot{\varepsilon} = 10^{-3}$ s^{-1} to a depth of 7 µm using a 120-µm diamond flat punch tip. For all experiments, the effective Young's modulus was approximated by the loading slope of each linear stress–strain regime.

Supporting Information

Supporting Information is available from the Wiley Online Library or from the author.

Acknowledgements

The authors gratefully acknowledge financial support from the Office of Naval Research Award N00014-22-1-2384.

Conflict of Interest

The authors declare no conflict of interest.

Keywords

additive manufacturing, anisotropy, biomimetic, machine learning, scaffold design

Received: August 11, 2023
Revised: January 8, 2024
Published online:

[1] M.-H. Sun, S.-Z. Huang, L.-H. Chen, Y. Li, X.-Y. Yang, Z.-Y. Yuan, B.-L. Su, *Chem. Soc. Rev.* **2016**, *45*, 3479.
[2] M. Sun, C. Chen, L. Chen, B. Su, *Front. Chem. Sci. Eng.* **2016**, *10*, 301.
[3] S. Dutta, A. Bhaumik, K. C.-W. Wu, *Energy Environ. Sci.* **2014**, *7*, 3574.
[4] S. J. Hollister, *Nat. Mater.* **2005**, *4*, 518.
[5] E. Cuce, P. M. Cuce, C. J. Wood, S. B. Riffat, *Renewable Sustainable Energy Rev.* **2014**, *34*, 273.
[6] A. Vyatskikh, A. Kudo, S. Delalande, J. R. Greer, *Mater. Today Commun.* **2018**, *15*, 288.
[7] D. J. Wales, J. Grand, V. P. Ting, R. D. Burke, K. J. Edler, C. R. Bowen, S. Mintova, A. D. Burrows, *Chem. Soc. Rev.* **2015**, *44*, 4290.
[8] L. B. Hu, C. Savidge, D. M. Rizzo, N. Hayden, J. W. Hagadorn, M. Dewoolkar, *J. Mater. Civ. Eng.* **2013**, *25*, 1803.
[9] V. Torres-Costa, R. J. Martin-Palma, in *Porous Silicon for Biomedical Applications* (Ed.: H. A. Santos), Woodhead Publishing Ltd., Sawston, UK **2014**, pp. 185–222.
[10] N. S. Mustafa, N. H. Akhmal, S. Izman, M. H. Ab Talib, A. I. M. Shaiful, M. N. B. Omar, N. Z. Yahaya, S. Illias, *Polymers* **2021**, *13*, 1584.
[11] C. Lautensack, S. Zuyev, *Adv. Appl. Probab.* **2008**, *40*, 630.
[12] C. Redenbach, I. Shklyar, H. Andrä, *Int. J. Eng. Sci.* **2012**, *50*, 70.
[13] S. Cai, J. Xi, *Comput.-Aided Des.* **2008**, *40*, 1040.

[14] J. Wu, C. C. L. Wang, X. Zhang, R. Westermann, *Comput.-Aided Des.* **2016**, *80*, 32.
[15] A. Vidyasagar, S. Krödel, D. M. Kochmann, *Proc. R. Soc. A* **2018**, *474*, 20180535.
[16] F. V. Senhora, E. D. Sanders, G. H. Paulino, *Adv. Mater.* **2022**, *34*, 2109304.
[17] C. M. Portela, A. Vidyasagar, S. Krodel, T. Weissenbach, D. W. Yee, J. R. Greer, D. M. Kochmann, *Proc. Natl. Acad. Sci. U. S. A.* **2020**, *117*, 5686.
[18] A. Guell Izard, J. Bauer, C. Crook, V. Turlo, L. Valdevit, *Small* **2019**, *15*, 1903834.
[19] C. M. Elliott, in *Math. Models Phase Change Probl*, (Ed.: J. F. Rodrigues), Birkhäuser, Basel, **1989**, pp. 35–73.
[20] J. W. Cahn, J. E. Hilliard, *J. Chem. Phys.* **1958**, *28*, 258.
[21] J. W. Cahn, *Acta Metall.* **1961**, *9*, 795.
[22] C. Soyarslan, S. Bargmann, M. Pradas, J. Weissmüller, *Acta Mater.* **2018**, *149*, 326.
[23] Y. Yang, X. Song, X. Li, Z. Chen, C. Zhou, Q. Zhou, Y. Chen, *Adv. Mater.* **2018**, *30*, 1706539.
[24] S. Frølich, J. C. Weaver, M. N. Dean, H. Birkedal, *Adv. Eng. Mater.* **2017**, *19*, e201600848.
[25] M. Wehner, R. L. Truby, D. J. Fitzgerald, B. Mosadegh, G. M. Whitesides, J. A. Lewis, R. J. Wood, *Nature* **2016**, *536*, 451.
[26] Senhora, F. V., Sanders, E. D., Paulino, G. H., *Adv. Mater.* **2022**, *34*, 2109304.
[27] D. Gu, X. Shi, R. Poprawe, D. L. Bourell, R. Setchi, J. Zhu, *Science* **2021**, *372*, eabg1487.
[28] M.-T. Hsieh, B. Endo, Y. Zhang, J. Bauer, L. Valdevit, *J. Mech. Phys. Solids* **2019**, *125*, 401.
[29] M.-T. Hsieh, M. R. Begley, L. Valdevit, *Mater. Des.* **2021**, *207*, 109838.
[30] A. du Plessis, C. Broeckhoven, I. Yadroitsava, I. Yadroitsev, C. H. Hands, R. Kunju, D. Bhate, *Addit. Manuf.* **2019**, *27*, 408.
[31] S. Kumar, S. Tan, L. Zheng, D. M. Kochmann, *npj Comput. Mater.* **2020**, *6*, 73.
[32] H. Kaur, H. S. Pannu, A. K. Malhi, *ACM Comput. Surv.* **2019**, *52*, 79.
[33] J. Hazrati Marangalou, K. Ito, M. Cataldi, F. Taddei, B. van Rietbergen, *J. Biomech.* **2013**, *46*, 2356.
[34] L. R. Meza, S. Das, J. R. Greer, *Science* **2014**, *345*, 1322.
[35] J. H. Ylostalo, *Cells* **2020**, *9*, 2178.
[36] Hgrobe, "Diatom_hg.jpg (5197×4252)," can be found under, https://upload.wikimedia.org/wikipedia/commons/d/d4/Diatom_hg.jpg, n.d.
[37] J. Sindhu, "Peacock_Plumage.jpg (5184×3174)," can be found under, https://upload.wikimedia.org/wikipedia/commons/c/c5/Peacock_Plumage.jpg, n.d.
[38] SecretDisc, "SEM_image_of_a_Peacock_wing,_slant_view_4.JPG (2560×2048)," can be found under, https://upload.wikimedia.org/wikipedia/commons/6/63/SEM_image_of_a_Peacock_wing%2C_slant_view_4.JPG, n.d.
[39] A. Boyde, *J. Anat.* **2003**, *203*, 173.
[40] Sylenius, "Cleaning_sponge_detail.jpg (3072×2304)," can be found under, https://upload.wikimedia.org/wikipedia/commons/a/ac/Cleaning_sponge_detail.jpg, n.d.